PCCP

PAPER

View Article Online
View Journal | View Issue

Cite this: *Phys. Chem. Chem. Phys.*, 2017, **19**, 31255

Role of spin–orbit interaction on the nonlinear optical response of $CsPbCO_3F$ using DFT

E. Narsimha Rao,[a] G. Vaitheeswaran, *[a] Ali H. Reshak [b] and S. Auluck[c]

Received 23rd August 2017,
Accepted 24th October 2017

DOI: 10.1039/c7cp05750d

rsc.li/pccp

We explore the effect of spin–orbit interaction (SOI) on the electronic and optical properties of $CsPbCO_3F$ using the full potential linear augmented plane wave method with the density functional theory (DFT) approach. $CsPbCO_3F$ is known for its high powder second harmonic generation (SHG) coefficient (13.4 times (d_{36} = 0.39 pm V^{-1}) that of KH_2PO_4 (KDP)). Calculations are done for many exchange correlation (XC) potentials. After the inclusion of SOI, the calculated Tran–Blaha modified Becke–Johnson (TB-mBJ) band gap of 5.58 eV reduces to 4.45 eV in agreement with the experimental value. This is due to the splitting of Pb p-states. Importantly, the occurrence of a band gap along the H–A direction (indirect) transforms to the H–H (direct) high symmetry points/direction in the first Brillouin zone. We noticed a large anisotropy in the calculated complex dielectric function, absorption, and refractive index spectra. The calculated static birefringence of 0.1049 and 0.1057 (with SOI) is found to be higher than that of the other carbonate fluorides. From the Born effective charge (BEC) analysis we notice that the Cs atom shows a negative contribution to birefringence whereas Pb, C, and F atoms show a positive contribution. In addition, we have also calculated the nonlinear optical $\chi^{(2)}_{ijk}(-2\omega;\omega,\omega)$ dispersion of a $CsPbCO_3F$ single crystal. We found that d_{11} = d_{12} = 4.35 pm V^{-1} at 1064 nm, which is 11.2 times higher than d_{36} of KDP. The origin of the highly nonlinear optical susceptibility dispersion of $CsPbCO_3F$ is explained. Overall, our results are in agreement with experiments and it is obvious from the present study that $CsPbCO_3F$ is a direct band gap, large second harmonic generation, and good phase matchable NLO crystal in the ultraviolet region.

1 Introduction

Nonlinear optical (NLO) polarization is an interesting phenomenon that arises from the application of highly intense laser radiation (in the order of > = 10^{10} V m^{-1}) on to the material.[1] However, before the invention of the laser, the optical fields of conventional sources were too weak to explore the optical nonlinearities. Based on the crystal symmetry it is possible to obtain second $\chi^{(2)}$ and third $\chi^{(3)}$ order nonlinear phenomena, Kerr effects, *etc.* for various materials.[2] In general, the conventional contracted d_{il} notations are used to represent these nonlinear susceptibilities of different classes of crystal symmetry. For example, under Kleinman's symmetry, the hexagonal crystal system of the D_{3h} class will have only one independent $d_{22} = -d_{21}$ SHG tensor component.[2] The strength of the nonlinearity will vary based on the chemical composition and the bonding environment which in turn decides the phase-matching conditions. These nonlinear effects have large scientific, medical, and industrial applications as they generate unknown coherent wavelengths in the ultraviolet (UV), deep-UV, and infrared (IR) regions. Among all the known NLO effects, second harmonic generation (SHG) is mostly utilized for generating different unknown wavelengths like those in the UV and deep-UV regions. Even though excimer lasers are used to emit isolated UV and deep-UV wavelengths with a high output power, compact and efficient solid-state lasers with suitable nonlinear crystals are still needed in this region.[1] Similarly, it is well known that many explosive materials show strong absorption in the 0.3–10 terahertz (THz) region of the optical spectrum.[3] In order to detect them for homeland security purposes, the development of generation and detection techniques for terahertz frequencies through NLO processes is very important and is an interesting field of research. To date, very few materials are commercially available to generate these frequencies with a desired band width. Hence the search for efficient new UV, deep-UV, and IR NLO materials is still a challenging task of research in the nonlinear optics domain. From the point of view of electronic properties, a better UV-NLO crystal for practical applications is expected to have larger nonlinear coefficients

[a] *Advanced Center of Research in High Energy Materials (ACRHEM), University of Hyderabad, Prof. C. R. Rao Road, Gachibowli, Hyderabad-500 046, Telangana, India. E-mail: vaithee@uohyd.ac.in; Tel: +91 40 23138709*
[b] *New Technologies-Research Center, University of West Bohemia, Univerzitni 8, 30614 Pilsen, Czech Republic*
[c] *Council of Scientific and Industrial Research – National Physical Laboratory, Dr K S Krishnan Marg, New Delhi 110012, India*

(>d_{36} of KDP), a wide band gap (>6.2 eV), and moderate birefringence (0.07) with a larger laser damage threshold value (>5 GW cm^{-2}).[4] Materials with P-O[8] (KH_2PO_4), I-O[7] ($LiIO_3$), Nb-O[5] ($LiNbO_3$), and B-O[6] (β-BaB_2O_4, LiB_3O_5, CsB_3O_5, $KBe_2BO_3F_2$, $Sr_2Be_2BO_7$, and $CsLiB_6O_{10}$) bonds have been extensively studied for this purpose.[1] But these materials possess their own drawbacks in generating coherent light such as a narrow band width, poor beam quality, lack of tunability, and relative difficulty of handling.[1]

For the past five years experimental and theoretical investigations[9–24] have suggested that carbonate fluorides (made up of C–O bonds) are promising polycrystalline NLO crystals for the generation of coherent light in the UV and deep-UV regions. Since 2011, the synthesis of non-centrosymmetric carbonate fluoride materials has accelerated to meet scientific and industrial needs. During the last five years, a few tens of carbonates (centrosymmetric and non-centrosymmetric) have been synthesised and their powder nonlinear optical responses to an applied external electric field (1064 nm) are reported in the literature. The novel CO_3F-based crystals reported to date are $ABCO_3F$ (A = K, Rb, Cs; B = Ca, Sr, Ba),[9] $CsPbCO_3F$,[10,11] $ATCO_3F$ (A = K, Rb; T = Zn, Cd),[12] $RbPbCO_3F$,[11] $RbMgCO_3F$,[13] $K_2Pb_3(CO_3)_3F_2$,[14] $KCdCO_3F$,[14] $Ca_2Na_3(CO_3)_3F$,[15] $MBeCO_3F$,[16] $MAlCO_3F_2$ (M = Li, Na, K, Rb, Cs),[16] $KPb_2(CO_3)_2F$,[17] $K_{2.70}Pb_5{\cdot}15(CO_3)_5F_3$,[17] $Cs_3Pb_2(CO_3)_3I$,[18] $KBa_2(CO_3)_2F$,[18] $RbBa_2(CO_3)_2F$,[18] $CsSrCO_3F$,[19] $Na_4Cd_3(CO_3)_4(OH)_2$,[21] and $ACdCO_3F$ (A = K and Rb).[22] Some carbonate crystals without fluorine have also been reported such as $Na_4La_2(CO_3)_5$,[23] $CsNa_5Ca_5(CO_3)_8$,[23] and $Pb_7O(OH)_3(CO_3)_3(BO_3)$.[20] Among all these reported carbonate fluorides, powder lead carbonate fluoride is found to show the largest SHG intensity (13.6 × d_{36} (0.39 pm V^{-1}) of KDP and 4 × that of $KSrCO_3F$).[10] All other crystals show a 1–5 times increase in the SHG coefficients with respect to d_{36} of the KDP crystal.

It is also important to notice from the literature that researchers are trying to use alkaline and alkaline-earth metal cations to eliminate the negative influence of d–d and f–f electronic transitions to the band gap[16] of carbonate fluorides. In addition, fluorine atoms' large electronegativity and its presence in carbonate fluorides have been found to be useful for producing a wide band gap, layered topology.[16] The absorption spectra studies and powder SHG measurements of carbonate fluorides also reveal that these materials possess wide band gaps above 6.0 eV and an absorption edge below 200 nm. These peculiar properties confirm the importance of carbonates in nonlinear optics for UV harmonic generation. In the process of innovation, $CsPbCO_3F$ is a recently synthesized optically active non-centrosymmetric crystal. Even though it possesses a smaller band gap (4.1 eV) than other carbonate crystals, it has the largest SHG coefficient (13.4 times that of KH_2PO_4) among the carbonates. In addition, it is transparent to light in the near-UV to middle-IR regions.[10] Due to the uniqueness of this NLO crystal, we have reported a detailed analysis of the structural, mechanical, vibrational, and thermodynamic properties in our previous work.[24] Our analysis revealed the soft (bulk modulus (B) = 41 GPa) and ductile (B/shear modulus (G) is >1.75) nature of $CsPbCO_3F$ with a high thermal conductivity (32.430 W m^{-1} K^{-1}).[24] We further noticed a need to explore the electronic and optical properties of $CsPbCO_3F$ in detail. It is important to synthesise this crystal with a larger size (few centimetres) and to alter the band gap and hence the reported preliminary experimental data is not sufficient alone. In the present work we have focused on qualitative analysis of the electronic, linear, and nonlinear optical properties of this novel material. Even though there are few theoretical reports on electronic band structure calculations in the literature, to the best of our knowledge the role of SOI (due to the presence of Pb & Cs) on various optoelectronic properties has not been studied. In general, for second-row transition metals and heavier elements, the role of SOI is not negligible.[25] Moreover, we should emphasize that the reported value of the SHG of $CsPbCO_3F$ is measured for a powder sample without considering the influence of the packing structural units. Hence, we have focused on the calculation of the SHG of $CsPbCO_3F$ taking into account the influence of the packing structural units using the full-potential method. According to the Chens' group theory,[44] the overall SHG response of a crystal is the geometrical superposition of the second order susceptibilities. Therefore, the packing structural units will also influence the macroscopic SHG coefficients. The high SHG arises due to the strong interactions between the structural units. Therefore, the novelty and the aim of this work are to carry out qualitative and quantitative investigation to report the SHG values and the details of the SHG tensors of a $CsPbCO_3F$ single crystal.

Hence in this work, we report the electronic, linear, and nonlinear optical susceptibility dispersion of $CsPbCO_3F$ by taking SOI into account. The experimental crystal structure of $CsPbCO_3F$ is shown in Fig. 1 along with the iso-structural compounds $RbSrCO_3F$, $KCaCO_3F$, and $KSrCO_3F$ for comparison. Computational techniques utilized for the present calculations are presented in Section 2. In the results and discussion (Section 3), we discus the effect of SOI on the electronic band structure and bonding and on the linear optical properties such as the real and imaginary parts of the complex dielectric function, absorption spectra, refractive index, and birefringence. In the next section we explore the nonlinear optical response with respect to energy/frequency. Finally the conclusions are given in Section 4.

2 Calculation methods

For the present computational study, we have considered the experimental crystal parameters[10] as reported by Zou *et al.* $CsPbCO_3F$ crystallizes in the $P\bar{6}m2$ (hexagonal) non-centrosymmetric space group, with Z = 1 formula unit per unit cell having a volume (V) of 128.44 Å^3. The Wyckoff positions of atoms with an occupancy of 1 are as follows: Cs (0 0 0), C (0.3333 0.6667 0.5), F (0.6667 0.3333 0), Pb (0.6667 0.3333 0.5), and O (0.1961 0.392 0.5). We have used the full-potential linearized augmented plane wave (FP-LAPW) and local orbitals method through a density functional theory approach.[26] Here, the Kohn–Sham equations are solved by expanding the wave functions in the spherical harmonics form inside the atom spheres. Plane wave expansion is used in the interstitial regions of atoms inside the unit cell. We have used l_{max} = 10 for angular momentum expansion and $K_{max} \times R_{MT}$ = 7 as a plane wave cut-off

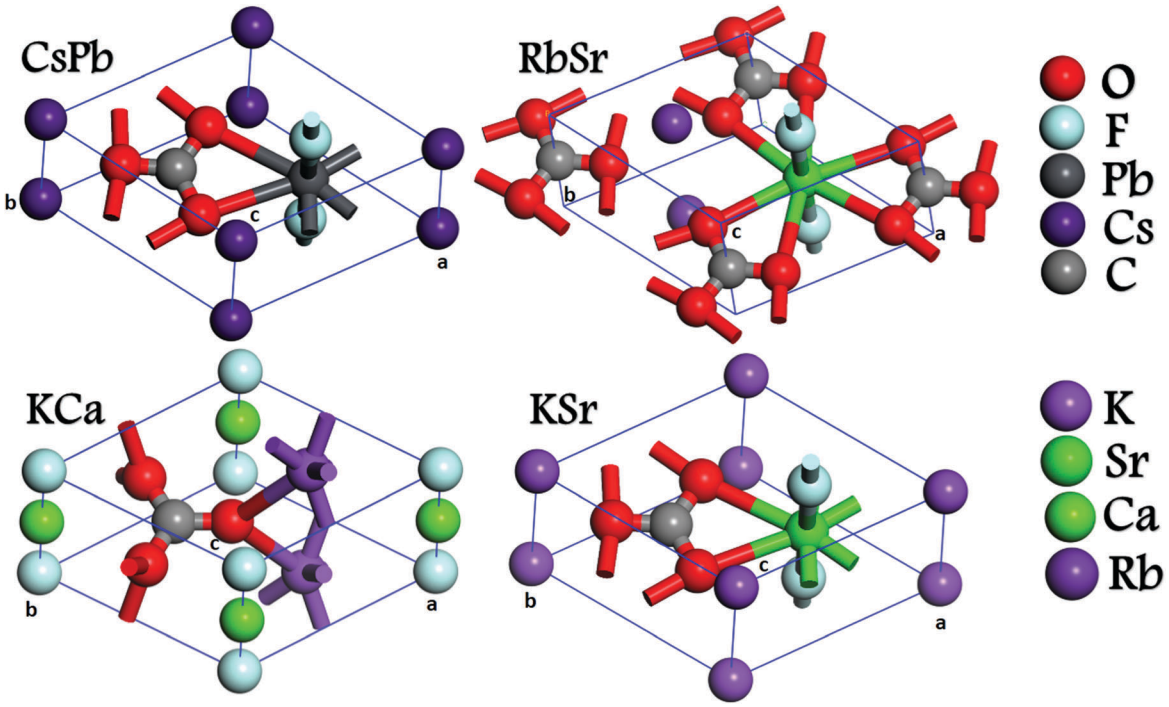

Fig. 1 Experimental[9,10] crystal structures of $CsPbCO_3F$, $RbSrCO_3F$, $KCaCO_3F$, and $KSrCO_3F$.

with 1000 k points to achieve self-consistency. Here $R_{[MT]}$ is the average muffin-tin (MT) radius and K_{max} is the wave function cut-off. The muffin-tin (MT) radii for different atoms are taken as 2.5 atomic units (a.u.) for Pb, 2.0 a.u. for Cs, 1.2 a.u. for O, 1.8 a.u. for F, and 1.1 a.u. for C atoms. The energy between successive iterations is converged to 0.0001 Ry and forces are minimized to 1 mRy $Bohr^{-1}$. The Monkhorst–Pack (MP) technique is used for Brillouin zone integrations. We used the Perdew–Burke–Ernzerhof (PBE,[32] PBESol[33]) and Tran–Blaha modified Becke–Johnson approach (TB-mBJ)[27] as an exchange correlation functional to extract the electronic band structures. A dense k-mesh with 1500 k-points was used in the first Brillouin zone to calculate the linear optical properties. To treat the interactions of heavier elements like Pb and Cs one needs to consider SOI during the calculations.[28] Therefore, we have performed electronic band structure and optical property calculations with and without SOI. In WIEN2k, spin–orbit (SO) effects are included *via* a second variational procedure to calculate the eigenvalues and eigenvectors using the scalar relativistic wave functions.[29] We used the second variation energy cut-off as 10.0 Ry. The optical properties are calculated using the optics package in WIEN2k. The complex second order nonlinear optical susceptibility tensor $\chi^{(2)}_{ijk}(-2\omega;\omega,\omega)$ has been discussed earlier and we refer the interested reader to ref. 40–48. It can be generally written as:

$$\chi^{(ijk)}_{inter}(-2\omega;\omega,\omega) = \frac{e^3}{\hbar^2}\sum_{nml}\int\frac{d\vec{k}\;\vec{r}^{\,i}_{nm}\{\vec{r}^{\,j}_{ml}\vec{r}^{\,k}_{ln}\}}{4\pi^3(\omega_{ln}-\omega_{ml})} \times\left\{\frac{2f_{nm}}{\omega_{mn}-2\omega}+\frac{f_{ml}}{\omega_{ml}-\omega}+\frac{f_{ln}}{\omega_{ln}-\omega}\right\} \quad (1)$$

$$\chi^{(ijk)}_{intra}(-2\omega;\omega,\omega) = \frac{e^3}{\hbar^2}\int\frac{d\vec{k}}{4\pi^3}\left[\sum_{nml}\omega_{nm}\vec{r}^{\,i}_{nm}\{\vec{r}^{\,j}_{ml}\vec{r}^{\,k}_{ln}\}\frac{f_{nl}}{\omega_{ln}{}^2(\omega_{ml}-\omega)} + \frac{f_{lm}}{\omega_{ml}{}^2(\omega_{ml}-\omega)} - 8i\sum_{nm}\frac{f_{nm}\vec{r}^{\,i}_{nm}\left\{\vec{\Delta}^{j}_{mn}\vec{r}^{\,k}_{nm}\right\}}{\omega_{mn}{}^2(\omega_{mn}-2\omega)} + 2\sum_{nml}\frac{f_{nm}\vec{r}^{\,i}_{nm}\{\vec{r}^{\,j}_{ml}\vec{r}^{\,k}_{ln}\}(\omega_{ml}-\omega_{ln})}{\omega_{mn}{}^2(\omega_{mn}-2\omega)}\right] \quad (2)$$

$$\chi^{(ijk)}_{mod}(-2\omega;\omega,\omega) = \frac{e^3}{2\hbar^2}\int\frac{d\vec{k}}{4\pi^3}\left[\sum_{nml}\frac{f_{nm}}{\omega_{mn}{}^2(\omega_{mn}-\omega)} \times\{\omega_{nl}\vec{r}^{\,i}_{lm}\}\{\vec{r}^{\,j}_{mn}\vec{r}^{\,k}_{nl}-\omega_{lm}\vec{r}^{\,i}_{nl}\}\{\vec{r}^{\,j}_{lm}\vec{r}^{\,k}_{mn}\} - i\sum_{nm}\frac{f_{nm}\vec{r}^{\,i}_{nm}\left\{\vec{r}^{\,j}_{mn}\vec{\Delta}^{\,k}_{mn}\right\}}{\omega_{mn}{}^2(\omega_{mn}-\omega)}\right] \quad (3)$$

From these formulae we notice that there are three major contributions to $\chi^{(2)}_{ijk}(-2\omega;\omega,\omega)$: the inter-band transitions $\chi^{(ijk)}_{inter}(-2\omega;\omega,\omega)$, the intra-band transitions $\chi^{(ijk)}_{intra}(-2\omega;\omega,\omega)$, and the modulation of inter-band terms by intra-band terms $\chi^{(ijk)}_{mod}(-2\omega;\omega,\omega)$, where $n \neq m \neq l$. Here n denotes the valence states, m denotes the conduction states, and l denotes all states ($l \neq m, n$). There are two kinds of transition that can take place; one of them (v c c′) involves one valence band (v) and two conduction bands (c and c′), and the second transition (v v′ c) involves two valence bands (v and v′) and one conduction band (c).

The symbols are defined as $\Delta^i_{nm}(\vec{k}) = \vartheta^i_{nn}(\vec{k}) - \vartheta^i_{mm}(\vec{k})$ with ϑ^i_{nm} being the i component of the electron velocity given as $\vartheta^i_{nm}(\vec{k}) = i\omega_{nm}(\vec{k})\vec{r}^{\,i}_{nm}(\vec{k})$ and $\{\vec{r}^{\,i}_{nm}(\vec{k})\vec{r}^{\,j}_{ml}(\vec{k})\} = 1/2(\vec{r}^{\,i}_{nm}(\vec{k})\vec{r}^{\,j}_{ml}(\vec{k}) + \vec{r}^{\,j}_{nm}(\vec{k})\vec{r}^{\,i}_{ml}(\vec{k}))$.

The position matrix elements between band states n and m, $\vec{r}^{i}_{nm}(\vec{k})$ are calculated from the momentum matrix element P^{i}_{nm} using the relation:[49] $\vec{r}^{i}_{nm}(\vec{k}) = \frac{P^{i}_{nm}(\vec{k})}{im\omega_{nm}(\vec{k})}$, with the energy difference between the states n and m given by $\bar{h}\omega_{nm} = \bar{h}(\omega_n - \omega_m)$. $f\omega_{nm} = f\omega_n - f\omega_m$ is the difference of the Fermi distribution functions. i, j, and k correspond to Cartesian indices. It has been demonstrated that only the one electron virtual transitions (transitions between one valence band state and two conduction band states (v c c′)) give a significant contribution to the second order tensor.[50] We ignore the virtual hole contribution (transitions between two valence band states and one conduction band state (v v′ c)) because it was found to be negative and more than an order of magnitude smaller than the virtual electron contribution for this compound. For simplicity we denote $\chi^{(2)}_{ijk}(-2\omega;\omega,\omega)$ by $\chi^{(2)}_{ijk}(\omega)$.

It is clear that from formulae (1)–(3) that the energy gap comes in the denominator. Hence the nonlinear optical properties are very sensitive to the energy gap. Therefore, to obtain accurate results it is necessary to use TB-mBJ exchange correlation potentials. We have applied the scissors correction to bring the value of the calculated energy gap to match the measured gap by rigidly shifting the conduction/valence bands. It has been found that the scissors corrections has a profound effect on the magnitude of the complex second order nonlinear optical susceptibility tensors.

3 Results and discussion

3.1 Electronic band structure and density of states

It is very important to understand the bonding and optically transparent region of a NLO material correctly by means of predicting the exact energy band gap. Since $CsPbCO_3F$ is a recently synthesized carbonate fluoride crystal, there are very few reports available in the literature on the electronic properties which explain the fundamental structure–property co-relationship. $CsPbCO_3F$ is a layered, phase-matchable hexagonal crystal with lattice parameters a = 5.3888 Å and c = 5.1071 Å.[10] For the first time Zou's group reported the experimental band gap of $CsPbCO_3F$ from UV-vis diffuse reflectance spectra as 4.15 eV. They have also reported a theoretical band gap (using the PBE functional) of 3.35 eV using CASTEP software.[10] This deviation was obtained due to the fact that the GGA normally underestimates the band gap by around 50%. Later, Thao Tran's group also reported the band gap of the $CsPbCO_3F$ crystal as 3.31 eV by using the PBEsol functional as implemented in the total energy code VASP.[4] Even though there are differences in the $CsPbCO_3F$ crystal structures reported by Zou and Thao Tran, they possess a similar band gap difference when compared with the experimental value. More recently, in 2016, Qun Jing *et al.* reported a theoretical optical band gap of 3.43 eV and 4.0 eV by using the PBE and modified Becke–Johnson (mBJ) methods as implemented in the FP-LAPW code.[30] In this work, the optical properties were calculated with the PBE functional after adding the scissors correction. Moreover, the mBJ optical band gap was obtained by adjusting the c-parameter to 1.2, which is a relatively expensive calculation compared to the default TB-mBJ functional. Overall, all the theoretically reported values so far were obtained without considering the effect of SOI. Our calculations remove this drawback.

We have considered the experimental crystal structure reported by Zou *et al.* and minimized the total energies and forces. Initially, we performed the electronic band gap calculations with the PBE,[32] PBESol,[33] and TB-mBJ[27] functionals using the FP-LAPW method. Due to the presence of heavier elements like Pb and Cs, we have incorporated SOI.[31]

The obtained band gap values along with previously reported theoretical and experimental results are presented in Table 1. The results obtained without the inclusion of spin–orbit effects with the PBE (3.59 eV) and PBEsol (3.48 eV) functionals show good improvement over the previously reported values.[10,11,27] The improved band gap is obtained with the default TB-mBJ functional (5.58 eV). However all these values deviate from the experimental value of ~4.1 eV. The underestimation of the band gap due to GGA functionals can be attributed to the lack of derivative discontinuities of the XC potential with respect to occupation number. But a more sophisticated semi-local DFT method like TB-mBJ in the present case also shows large deviation (~30%) when compared to the experimental band gap, which clearly suggests to us that we should re-look at the physical properties of the present compound. The accuracy of the TB-mBJ band gap of 4.0 eV[30] reported with the c-parameter variation method without the spin–orbit effect needs to be re-verified.

However, after SOI is taken into consideration, we found a considerable reduction in the calculated band gap. The gap values are 3.03 eV (PBE), 2.94 eV (PBEsol), and 4.45 eV (default mBJ). Therefore we can conclude that the TB-mBJ functional with the inclusion of SOI gives an improved band gap value that is in good agreement with the experimental data (4.15 eV[10] and 4.1 eV[11]). This indicates that treating SOI with the mBJ functional is more efficient than using other functionals in the present case. It is clear from Table 1 that the differences in the predicted band gaps before and after the inclusion of spin–orbit effects are as follows: with PBE and PBEsol: ~0.5 eV; with TB-mBJ: ~1 eV. This change can be attributed to the limitations of PBE and PBEsol functionals and the improved performance of the TB-mBJ functional.[34] Moreover, since it is known that $CsPbCO_3F$ possesses considerable van der Waals (vdW) interactions,[24] the accuracy of the present obtained band gap

Table 1 Calculated energy band gaps (in eV) of $CsPbCO_3F$ with and without the inclusion of SOI at an experimental volume. Results are compared with previously reported data

Functional	Present		Previous
	Without	With	Without
PBE	3.59	3.03	3.35,[10] 3.43[30]
PBEsol	3.48	2.94	3.31[11]
TB-mBJ	5.58	4.45	4.0[30]
Experiment	—	—	4.15,[10] 4.1[11]

values with respect to the experimental value may be further improved by incorporating van der Waals (vdW) interactions along with spin–orbit interactions. Since it is well known that the change in lattice parameters along with spin–orbit effects may influence the interactions between the constituent atoms,[35] it is better to also take vdW interactions into account. However since the TB-mBJ + SOI band gap results already show reasonable agreement with experiments in the present case, we did not check the actual effect of vdW interactions along with SOI.

We have calculated the band structure along symmetry directions in the first Brillouin zone with/without SOI and this is shown in Fig. 2. The results show considerable splitting in the energy levels both in the valence band (in the −5 eV to −10 eV and −15 eV to −17.5 eV regions) and in the conduction band (in the 5 eV to 10 eV region). These regions are shown in Fig. 2 separately. The 1 eV downward shift of energy bands in the bottom of the conduction band towards the Fermi level is seen clearly. Importantly, after the inclusion of SOI, the band gap which occurs in the H–A direction is transformed to the H high symmetry point *i.e.* an indirect to direct band gap. It is well known that indirect band gap materials are inefficient at emitting light.

In order to understand the individual atomic contribution to the splitting of energy levels, we have calculated the total and partial density of states (DOS) with/without SOI at the TB-mBJ level. The results are shown in Fig. 4. It is clear from the plots that the top of the valence band is dominated by Pb-s, F-p, and O-p states before and after the inclusion of SOI. The F-s and F-p states are dominate in the bottom of the conduction band before the inclusion of SO effects, while F-p and F-s states are dominate in the bottom of the conduction band with SOI. It is also found from Fig. 4 that the p-states corresponding to the lead atom are shifted downwards by 1 eV to the bottom of the conduction band whereas no changes were observed in the top of the valence band near the Fermi level. We have also noticed from the PDOS plots that a strong covalency exists between carbon and oxygen atoms in the CO_3 group. Ionic bonding is also observed between Pb and F and Cs and between Pb and the CO_3 group. The same is observed from charge density plots plotted in the *xy* and *yz* planes as shown in Fig. 5. There is charge sharing between carbon and oxygen atoms, and Pb and F are found to form a dumbell shape. The charge around the Cs atom is spread in a spherical shape which confirms the presence of ionic bonding. For further understanding the lead atomic orbital contribution to the band structure around the Fermi level, we have performed fat-band analysis. Since the effect of Pb-p states is more crucial in this compound, we have plotted the Pb-total p(p_x + p_y, p_z) orbital contributions in Fig. 3. Here Fig. 3(a) and (b) show the clear contribution and splitting of the lead p-total states before and after the inclusion of SOI. In order to obtain details about the two downward shifted fat-bands in the conduction band (Fig. 3(b)), we have plotted the partial Pb-p state contribution separately. Fig. 3(c) and (d) show the p_x + p_y state and p_z state contributions to the energy band structure. It is clear from these figures that the bottom of the conduction band is occupied by p_x + p_y states but not by p_z states. The indirect to direct band gap transition arises due to p_x + p_y states alone and it can be observed only after the spin–orbit effects are taken into account.

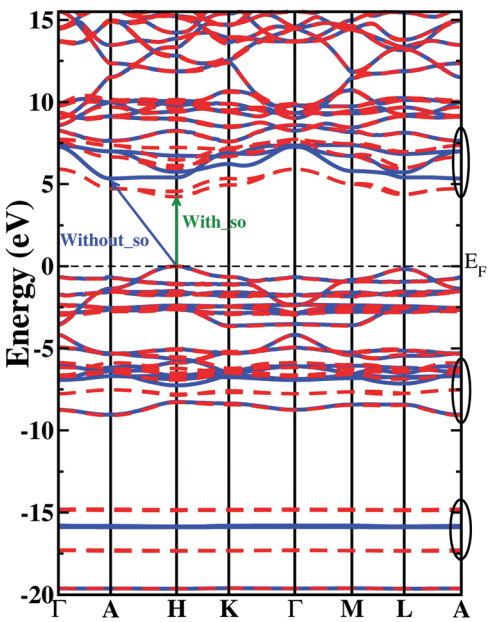

Fig. 2 Calculated TB-mBJ electronic band structure with and without spin–orbit interaction effects of $CsPbCO_3F$ at an experimental crystal structure volume.

3.2 Linear optical properties and birefringence

Until now there are no detailed experimental & theoretical reports available in the literature on the linear optical properties of $CsPbCO_3F$. In this section, we report calculations of the linear optical properties with/without SOI along with the TB-mBJ functional. The optical properties can be described in terms of the real and imaginary parts of the dielectric function as $\varepsilon(\omega) = \varepsilon_1(\omega) + i\varepsilon_2(\omega)$. As the studied compound crystallizes with a hexagonal crystal structure, there are two possible non-zero components of the dielectric tensor along the [1 0 0] and [0 0 1] directions. The imaginary part of the dielectric function ($\varepsilon_2(\omega)$) arises due to direct inter-band transitions and is calculated using a random-phase approximation.[36,37] Here, the small contribution of indirect inter-band transitions arising due to phonon scattering is neglected.

$$\varepsilon_2(\omega) = \left(\frac{4\pi^2 e^2}{m^2\omega^2}\right)\left(\sum_{i,j}\int_k \langle i|M|j\rangle^2 f_i(1-f_i) \times \delta(E_{j,k} - E_{i,k} - \omega)\mathrm{d}^3k\right). \quad (4)$$

Here i and j are the initial and final states and M is the dipole matrix. f_i and E_i are the Fermi distribution function and the energy of an electron in the ith state of the wave vector k. The real part of the dielectric function ($\varepsilon_1(\omega)$) is calculated using Kramers–Kronig transformations.[38]

$$\varepsilon_1(\omega) = 1 + \frac{2}{\pi}P\int_0^\infty \frac{\omega'\varepsilon_1(\omega')\mathrm{d}\omega'}{(\omega'^2 - \omega)} \quad (5)$$

The calculated complex dielectric function (real and imaginary parts) of lead carbonate with/without the SO effect is shown

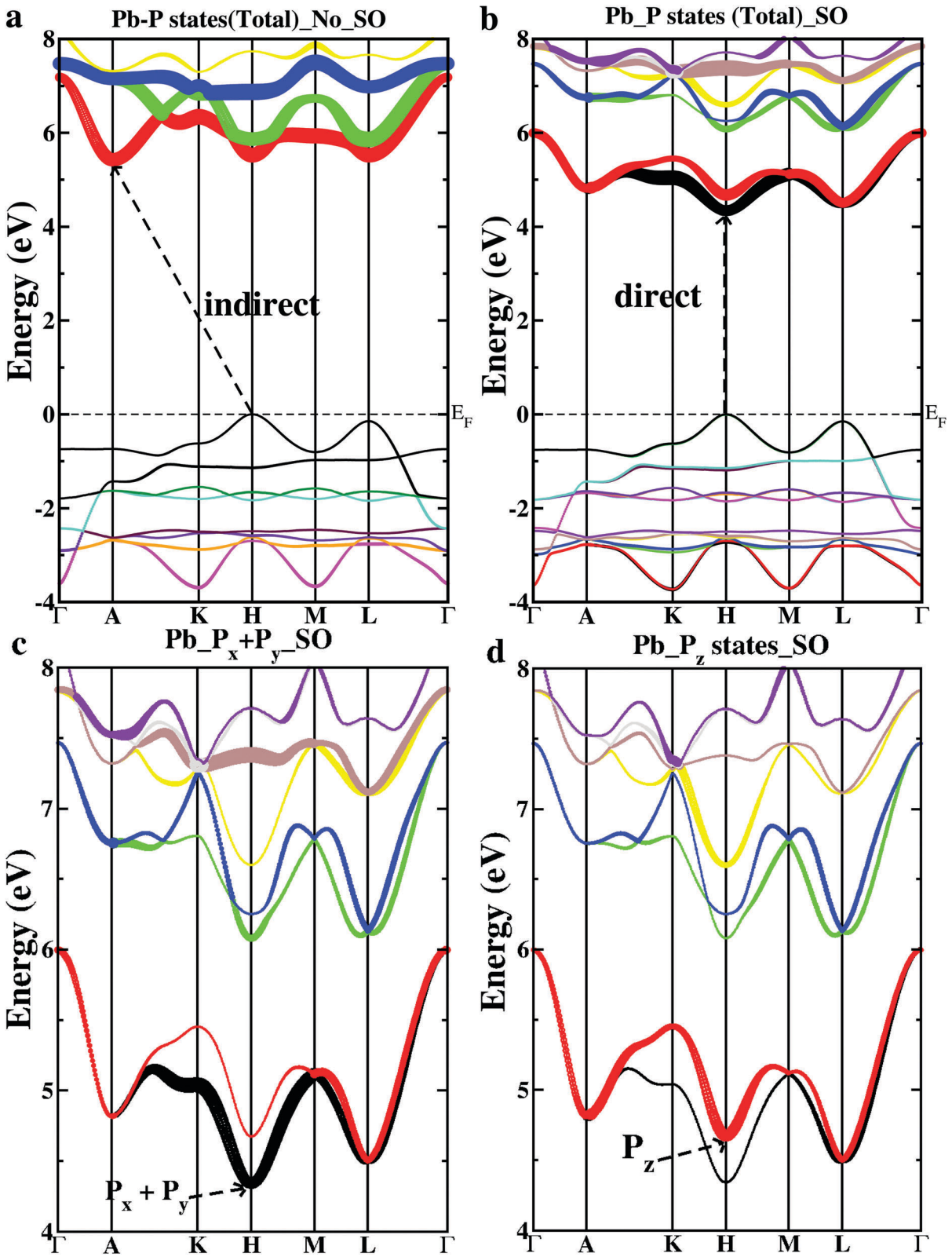

Fig. 3 Calculated partial electronic band structure of (a) Pb p-total states without SOI, (b) Pb p-total states with the inclusion of SOI, (c) $p_x + p_y$ states with SOI, and (d) p_z states with the SOI effects of $CsPbCO_3F$ at an experimental crystal structure volume using the TB-mBJ functional.

in Fig. 6. $\varepsilon_1(\omega)$ is shown in Fig. 6(a)–(c) and $\varepsilon_2(\omega)$ is plotted in Fig. 6(d)–(f). Here, Fig. 6(b) and (e) show $\varepsilon_1(\omega)$ and $\varepsilon_2(\omega)$ before SO effects and Fig. 6(c) and (f) show the results after the inclusion of SOI. For better visualisation, we have zoomed in

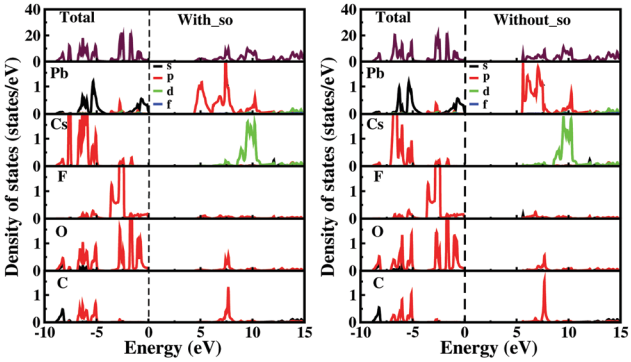

Fig. 4 Calculated DOS with and without spin–orbit interaction effects of $CsPbCO_3F$ at an experimental crystal structure volume.

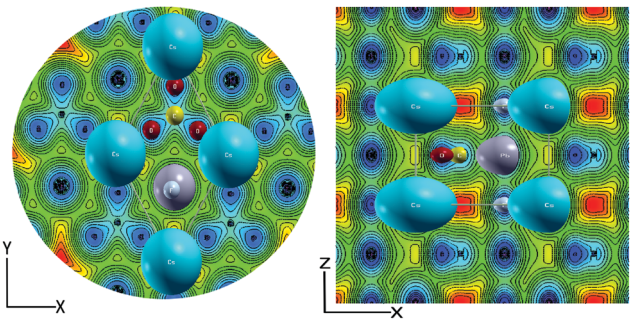

Fig. 5 Charge density difference plots of $CsPbCO_3F$ along the [1 1 0] and [1 0 1] planes from left to right.

and plotted the real and imaginary parts of the complex dielectric function on top of each other in Fig. 6(a) and (d). It can be seen from the plots that $CsPbCO_3F$ possesses large anisotropy in the dielectric constants along the [1 0 0] and [0 0 1] directions. Further observations on the spreading of the dielectric spectra with respect to energy (eV) leads to the following important conclusions. Firstly, the spectra obtained before the inclusion of the SO effect indicate that: (1) the high intensity peaks of ε_{xx} occur at energies (eV) of 6, 6.5, 9.2, 7.9, 8.5, 11.11, 12.0, and 13.5, respectively. A dip is observed at 9.5 eV with a magnitude of −1.47 for ε_{xx}; (2) for ε_{zz}, high intensity peaks occur at energies (eV) of 5.6, 8.2, 6.5, 11, 11.7, 10.0, 9.5, and 12.5, respectively; (3) overall, up to 7.25 eV ε_{xx} is dominant; from 7.25 to 8.25 eV ε_{zz} is dominant; from 8.25 to 9.25 eV ε_{xx} is dominant; and after that ε_{zz} shows a dominant nature. Secondly, the spectra after the inclusion of SO effects show that: (1) ε_{xx} occurs at energies (eV) of about 5.0, 5.7, 7.2, 9.0, 8.1, 11.6, 11.1, and 10.5. The dip of ε_{xx} occurs at 9.5 eV with a magnitude of −1.3; (2) ε_{zz} high intensity peaks occur at energies (eV) of about 4.9, 5.9, 7.5, 6.3, 8.7, 11, 10.5, 11.7, and 12.5; (3) up to 9 eV ε_{xx} is dominant and after that ε_{zz} is dominant. In conclusion, after SOI is taken into account, the ε_{xx} component shows a significantly higher value than ε_{zz} in the lower energy regions, whereas mixed behaviour of ε_{xx} and ε_{zz} was observed without the inclusion of SOI. Thus, these differences in the findings of the dielectric constants confirm the crucial role of SO effects in the optical properties of $CsPbCO_3F$. For further

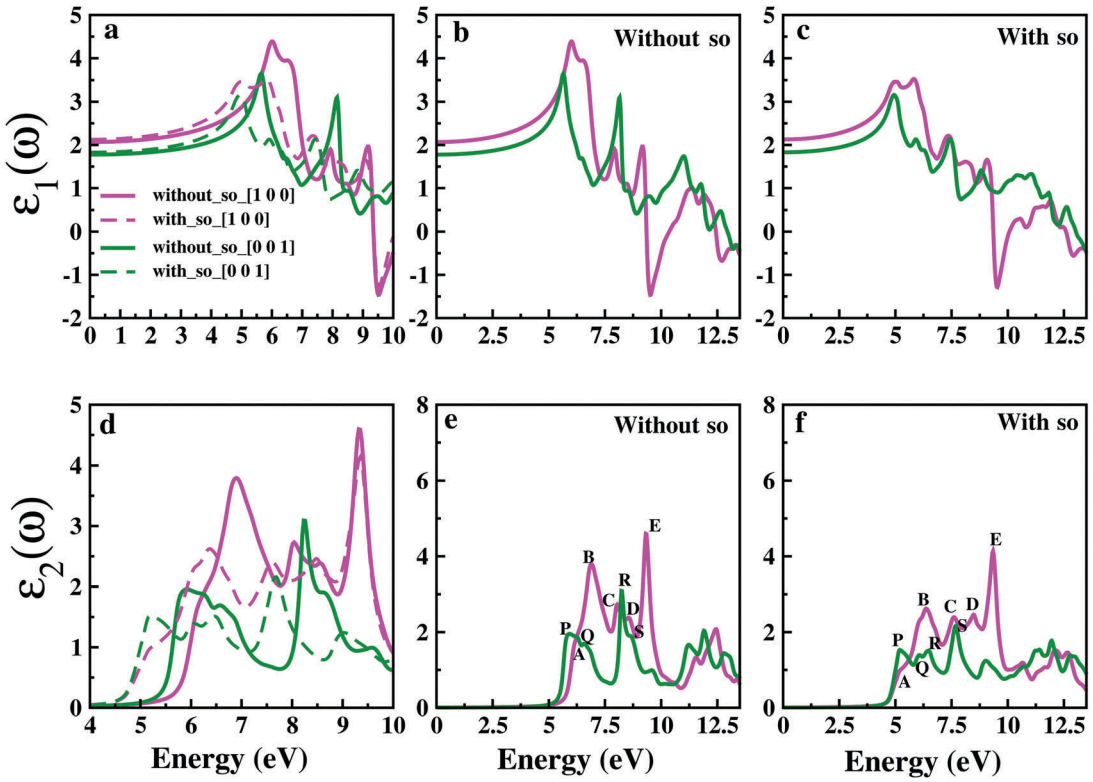

Fig. 6 Calculated real and imaginary parts of the complex dielectric function with and without SOI effects of $CsPbCO_3F$ at an experimental crystal structure volume.

Table 2 The optical transitions of $CsPbCO_3F$ before and after the inclusion of spin–orbit interactions observed from the imaginary part of the dielectric function and the TB-mBJ band structure

Direction	[1 0 0]				[0 0 1]			
Peak	A	B	C	D	P	Q	R	S
Before SO	6.3	6.9	8.0	8.5	5.9	6.6	8.2	8.6
After SO	5.2	6.4	7.6	8.5	5.2	6.0	6.5	7.7

Table 3 Linear optical properties such as the absorption coefficient ($\times 10^4$ cm^{-1}), refractive indices, and birefringence of $KCaCO_3F$, $KSrCO_3F$, and $RbSrCO_3F$

	$\varepsilon_1^{[100]}(\omega)$	$\varepsilon_1^{[001]}(\omega)$	$\alpha^{[100]}(\omega)$	$\alpha^{[001]}(\omega)$	n_0	n_e	Δn $(n_e - n_o)$
Before SO	2.12	1.82	73.16	40.8	1.43759	1.33270	0.10489
After SO	2.06	1.77	50.81	25.03	1.45832	1.35263	0.10569

analysis of possible optical transitions, the maximum intensity peaks in the imaginary part of the dielectric function plot (Fig. 6(e) and (f)) are labelled as A, B, C, and D along the *X*-direction and P, Q, R, and S along the *Z*-direction respectively. The positions of these peaks along two crystallographic directions [1 0 0] and [0 0 1] are tabulated in Table 2. From Table 2 it is clear that after the inclusion of SOI, all of the peaks show a considerable red shift. Similarly, other linear optical properties such as the absorption ($\alpha(\omega)$) and refractive indices ($n(\omega)$) are calculated and shown in Fig. 7. The corresponding static values of dielectric constants, absorption coefficients, ordinary n_0 and extraordinary n_e refractive indices, and birefringence ($n_e - n_0$) values are shown in Table 3. Our results show that all the linear optical property spectra show a red shift with slight intensity variations.

For deeper level of understanding of the optical response of $CSPbCO_3F$, we have analysed the possible optical transitions from the valence band to the conduction band states by utilising PDOS information (Fig. 4). It is clear from the PDOS plots that the Pb(s), O(s), and F(p) states are dominate in the VBM (−1 eV to the Fermi level) and these states are unaffected by the inclusion of SOI. In the deep valence band below −2 eV, spreading in the DOS peaks of the Pb(p), Cs(d), F(p), O(p), and C(p) states is clearly seen, whereas in the conduction band minimum, before including spin–orbit effects, the Pb(p), Cs(d,p), F(s,p), C(p,s), and O(s,p) states are dominant. After the inclusion of SOI, a clear difference in the dispersion of the DOS in the Pb(p), F(p,s), O(p), C(s, p), and Cs(d,p) states is observed. It is also noticed that all of the states are red-shifted in the bottom of the conduction band by approximately 1 eV as follows: O (1.15 eV), Pb (1.14 eV), Cs (1.02 eV), F (0.91 eV), and C (0.79 eV). Hence these observed differences in the PDOS will lead to changes in the optical properties. Based on the selection rules, we have explained the possible optical transitions (from the valence band to the conduction band) for the high intensity peaks in the [1 0 0] crystallographic direction. The results before and after the inclusion of SOI are tabulated in Table 4. Because of the changes in the DOS spreading, the optical transitions also

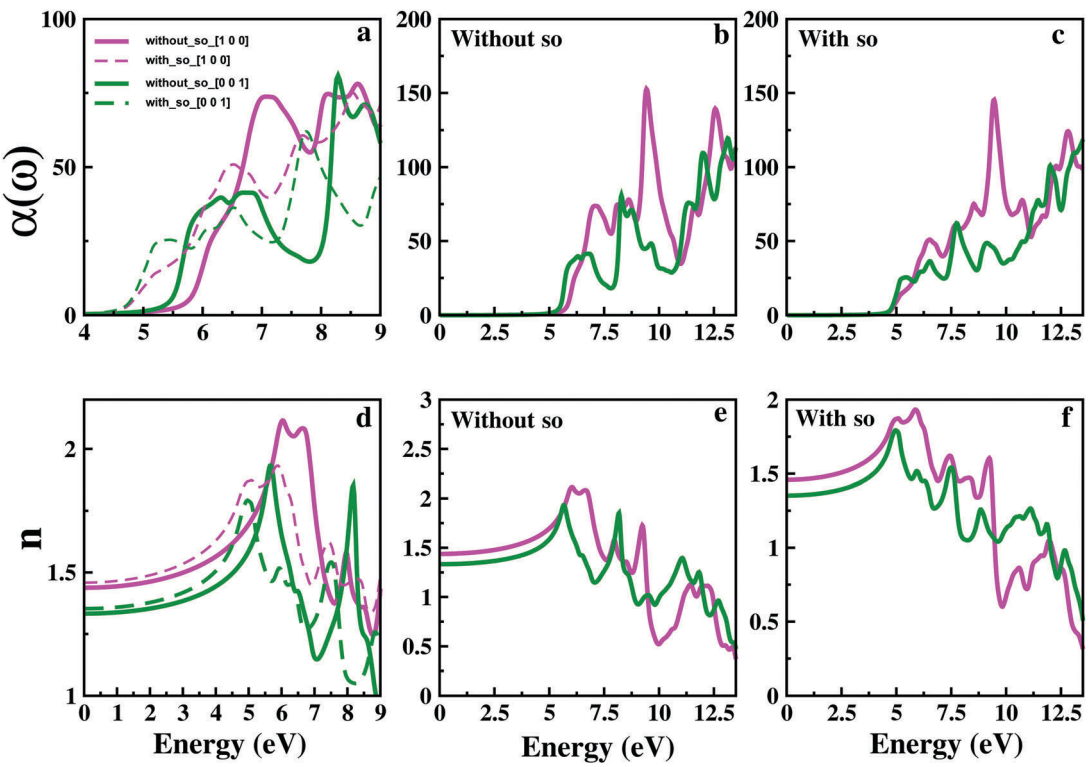

Fig. 7 Calculated refractive index and absorption spectra with and without spin–orbit interaction effects of $CsPbCO_3F$ at an experimental crystal structure volume.

Table 4 The optical transitions of $CsPbCO_3F$ derived from the top of the valence band to the conduction band observed from the imaginary part of the dielectric function along the [1 0 0] direction

Peaks	Transitions
Before SO	
A	Pb(s) to F(p)/O(p)/C(p)/Cs(p); O(P) to F(s)/Cs(d)/Cs(s)/Pb(s); F(P) to O(s)/Cs(d)/Cs(s)/Pb(s)
B	Pb(s) to F(p)/C(p)/O(p)/Cs(p); O(P) to Cs(d)/F(s)/Cs(s)/Pb(d); F(P) to Cs(d)/O(s)/Cs(s)/Pb(d)
C	Pb(s) to O(p)/C(p)/F(p)/Cs(p); O(P) to F(s)/Cs(s)/Pb(d)/Cs(d); F(P) to Cs(d)/Pb(d)/Cs(s)
D	Pb(s) to O(p)/C(p)/F(p)/Cs(p); O(P) to Cs(d)/Cs(s)/F(s)/O(s)/Pb(s); F(P) to Cs(d)/Cs(s)/O(s)/Pb(d)
After SO	
A	Pb(s) to F(p)/O(p)/Cs(p); O(P) to F(s)/Pb(s)/Cs(d); F(P) to O(s)/Pb(s)/Cs(d)
B	Pb(s) to F(p)/O(p)/Cs(p); O(P) to F(s)/Cs(d); F(P) to O(s)/Cs(d)
C	Pb(s) to F(p)/C(p)/O(p)/Cs(p); O(P) to Cs(d)/Cs(s)/Pb(d); F(P) to Cs(d)/Cs(s)/Pb(d)
D	Pb(s) to F(p)/C(p)/O(p)/Cs(p); O(P) to Cs(d)/F(s)/Cs(s)/Pb(d); F(P) to Cs(d)/O(s)/Cs(s)/Pb(d)

showed considerable variations in the results. In particular, in the case of absorption peaks A and B, a Pb(s) to C(p) state transition is possible before the inclusion of SOI effects, but later this transition can not occur. This clearly shows the role of SOI in explaining the optical transitions of the lead carbonate NLO material in the UV region. Our further optical transition analysis of other high intensity absorption peaks is given in Table 4. Similar kinds of effects can possibly occur in the [0 0 1] crystallographic direction too.

The values of the ordinary and extraordinary refractive indices show an increment of 0.0246 in magnitude after the inclusion of SOI. Furthermore, the birefringence values at static, 1064 nm (1.165 eV), 532 nm (2.33 eV) are tabulated in Table 5 for future reference. The results of all the studied crystals show a linear increment in the birefringence values starting from static → 1064 nm → 532 nm. Overall, it is clear from the results that $CsPbCO_3F$ possesses the largest birefringence at the TB-mBJ level among all the studied carbonate fluoride crystals. There are slight differences between the birefringence values reported by Qun Jing *et al.*[30] at the GGA-PBE level using CASTEP and our calculated results of $CsPbCO_3F$. The reason for this deviation comes from the accuracy of the TB-mBJ functional in predicting the exact band gap with the inclusion of SOI in the present case. Besides this expected discrepancy in the results, both works end up proposing lead carbonate as a unique material among the reported carbonate NLO materials family to date. In order to explore the reasons behind the changes in the birefringence (Δn) values of $CsPbCO_3F$, we have calculated Δn from 300 nm to 1200 nm and this is shown in Fig. 8. We find that the birefringence of $CsPbCO_3F$ is higher than that of other isostructural carbonate compounds. To explore the birefringence more, we have calculated the change in the Born effective charge values along two crystallographic directions using our recent work.

Table 5 The birefringence of $CsPbCO_3F$ before and after the inclusion of spin–orbit interactions observed from the imaginary part of the dielectric function at the TB-mBJ level. For comparison, the birefringence of $ABCO_3F$ (A = K, Rb; B = Ca, Sr) is also calculated using our previous work[39]

@	Before	After	RbSr	KSr	KCa
Static	0.10489	0.10569	0.08878	0.09210	0.09660
1064 nm	0.10639	0.10734	0.09012	0.09343	0.09815
532 nm	0.11089	0.11231	0.09429	0.09767	0.10287

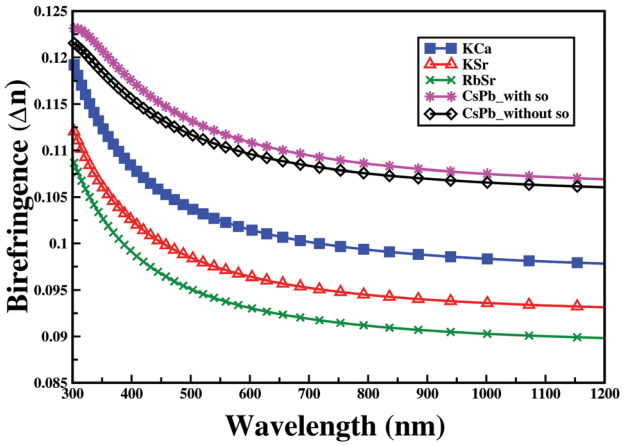

Fig. 8 Calculated birefringence of $CsPbCO_3F$ with spin–orbit interaction effects. $ABCO_3F$ (A = K, Rb; B = Ca, Sr) at an experimental crystal structure volume.

Table 6 The change in the Born effective charges along the *x* and *z* directions of different metal atoms of $CsPbCO_3F$ and $ABCO_3F$ (A = K, Rb; B = Ca, Sr)[24]

Atom	Δq	Atom	Δq	Atom	Δq	Atom	Δq
Cs	−0.28	Rb	−0.2	K	−0.11	K	−0.15
Pb	0.46	Sr	0.1	Sr	0.07	Ca	0.11
C	2.82	C	2.91	C	2.76	C	2.72
F	2.03	F	0.78	F	0.9	F	0.79

The results reveal that Cs and Rb negatively contribute to the birefringence, whereas Pb, C, and F show a positive contribution. Perhaps one can also clearly see the role of SOI on Δn of lead carbonate fluoride from Fig. 8. The reduction in the refractive indices (Fig. 7(b)) along the [1 0 0] and [0 0 1] directions and birefringence values after the inclusion of SO effects can be attributed to differences in the photo-induced inter-band transitions (Table 6).

3.3 Nonlinear optical susceptibility dispersion

$CsPbCO_3F$ crystallizes in a non-centrosymmetric structure resulting in the removal of the inversion symmetry which gives a non-zero second harmonic generation (SHG). The hexagonal structure with the space group $P\bar{6}m2$ allows seven non-zero

complex second order nonlinear optical susceptibility tensors $\chi_2^{(111)}(-2;\omega;\omega) = -\chi_2^{(122)}(-2;\omega;\omega) = \chi_2^{(133)}(-2;\omega;\omega) = \chi_2^{(212)}(-2;\omega;\omega) = \chi_2^{(221)}(-2;\omega;\omega) = \chi_2^{(313)}(-2;\omega;\omega) = \chi_2^{(331)}(-2\omega;\omega;\omega)$. Since the space group of $CsPbCO_3F$ belongs to the class $\bar{6}m2$, under the restriction of Kleinman's symmetry, only one set of independent SHG tensor components remains. Therefore, $\chi_2^{(111)}(-2\omega;\omega;\omega) = -\chi_2^{(122)}(-2\omega;\omega;\omega)$ completely defines the nonlinear optical properties of $CsPbCO_3F$.

The calculated $\chi_2^{(111)}(\omega)$ and $\chi_2^{(122)}(\omega)$ are shown in Fig. 9(a), in which $\chi_2^{(122)}(\omega)$ shows the same spectral features as $\chi_2^{(111)}(\omega)$ but with the opposite sign. The absolute value of $|\chi_2^{(ijk)}(\omega)|$ of $|\chi_2^{(111)}(\omega)|$ and $|\chi_2^{(122)}(\omega)|$ (Fig. 9(b)) reveals that both $\chi_2^{(111)}(\omega)$ and $\chi_2^{(122)}(\omega)$ present the same structural features with a second harmonic generation (SHG) value of about 4.7 pm V^{-1} at the static limit and 8.7 pm V^{-1} at λ = 1064 nm *i.e.* $d_{11} = d_{12}$ = 2.35 pm V^{-1} at the static limit and 4.35 pm V^{-1} at λ = 1064 nm. The latter is about 11.2 times that of the experimental value of the well-known KDP single crystals (d_{36} = 0.39 pm V^{-1})[51] and about a quarter of the experimental value of $KTiOPO_4$ (KTP) single crystals which exhibit a d_{36} value of about 16.9,[52] 16.75,[60] 16.65,[60] 15.4 ± 0.2,[54] 14.6 ± 1.0,[55] 17.4 ± 1.7,[56] 16.9 ± 3.3,[57] 16.9 ± 1.7,[58] 13.7,[53] and 10.6 ± 7.5.[59] Our calculated value also shows good agreement with the previous calculated results.[10] It has been reported that the estimated average NLO susceptibility $\langle d_{eff}\rangle_{exp}$ of $CsPbCO_3F$ is approximately 20 pm V^{-1}[11]. We should emphasize that this value is measured for a powder sample without taking into account the influence of the packing structural units.[11] It is important to highlight that, on the basis of anionic group theory,[44] the overall SHG response of a crystal is the geometrical superposition of the second order susceptibility. Thus, the packing of CO_3 structural units and the stereochemically active lone pair of Pb polyhedra can also influence the macroscopic SHG coefficients.[20] The larger SHG is due to the strong interactions of the stereo effect between Pb(II) cations and CO_3 triangle groups.[20] Moreover the $[CO_3]^-$ groups are the main contributors to the optical anisotropy; in addition, Pb^{2+} cations may also contribute to the optical anisotropy due to the repulsion interactions of the lone pairs of Pb^{2+} cations.[61] Furthermore, the high electron density configuration and strong anisotropy of C–O groups are the main contribution of CO_3 groups to the optical

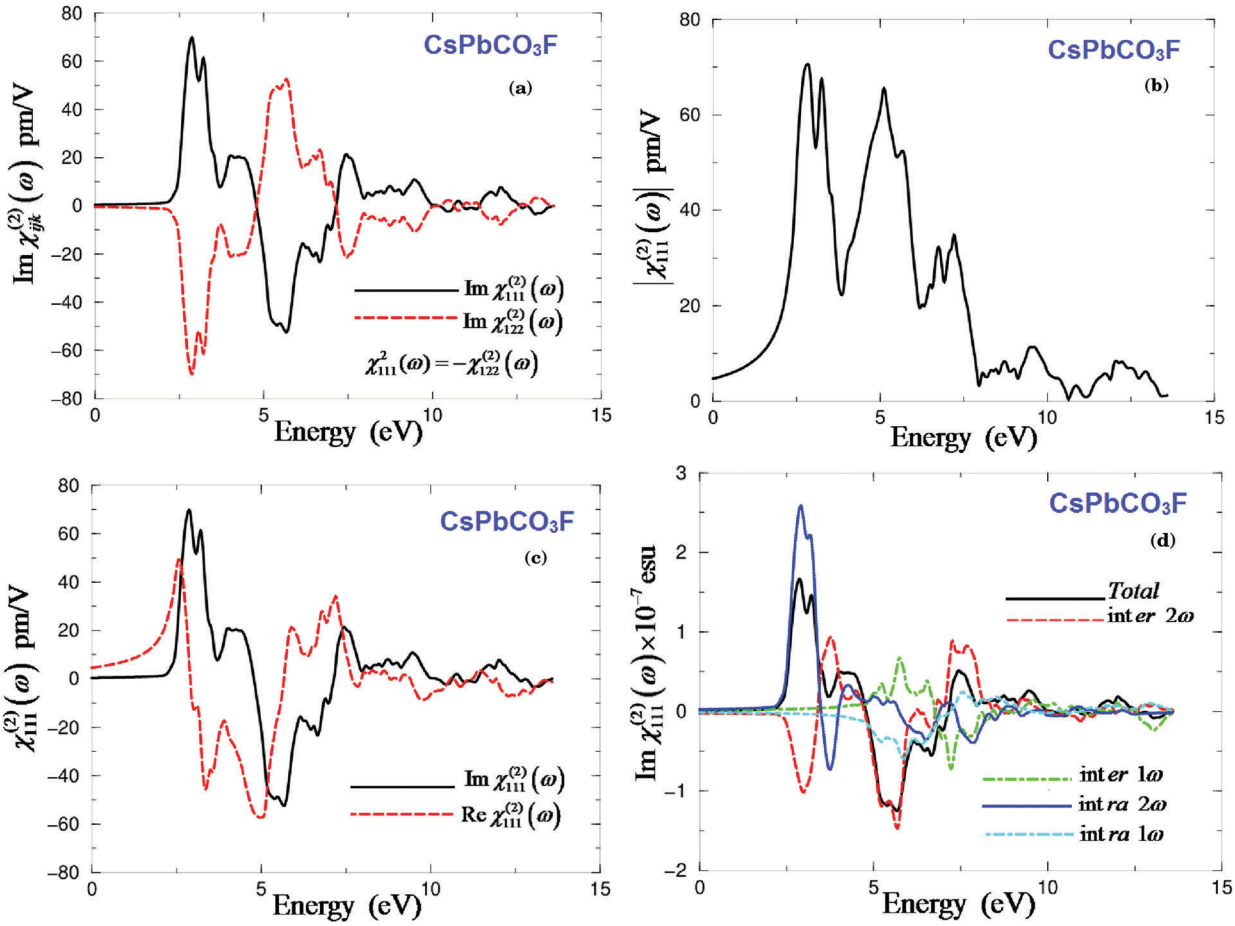

Fig. 9 (a) Calculated imaginary (dark solid curve, black line) and imaginary (light dashed curve, red line) spectra of $CsPbCO_3F$, which show $\chi_2^{(111)}(\omega) = -\chi_2^{(122)}(\omega)$; (b) calculated $|\chi_2^{(111)}(\omega)| = |\chi_2^{(122)}(\omega)|$ of $CsPbCO_3F$; (c) calculated imaginary (dark solid curve, black line) and real (light dashed curve, red line) spectra of $CsPbCO_3F$; (d) calculated total Im spectrum (dark solid curve, black line) along with the intra- (2)/(1) (light solid curve, blue line)/(light dashed dotted curve, cyan line) and inter- (2)/(1) (light long dashed curve, red line)/(light dotted curve, green line) band contributions of $CsPbCO_3F$, where all Im frequencies are multiplied by 10^{-7}, in esu units.

anisotropy (Fig. 5). The imaginary and real parts of $\chi_2^{(111)}(\omega)$ for $CsPbCO_3F$ are shown in Fig. 9(c). From the imaginary part we can see that the spectral futures of $\chi_2^{(111)}(\omega)$ exhibit a zero value below half of the band gap and slowly rise up after $\sim$2.2 eV since the 2ω resonance begins to contribute at energies above $\sim$2.2 eV (half of the band gap) due to E–2ω terms in the denominator of formulae (1)–(3). The ω resonance begins to contribute for energy values above the value of the fundamental band gap ($\sim$4.4 eV). At a low spectral range (less than $\sim$2.2 eV) the SHG optical spectra are dominated by the 2ω contributions. Beyond $\sim$4.4 eV (the fundamental gap) the major contribution comes from the ω term. To support this, we have plotted the $2\omega/\omega$ inter-/intra-band contributions to the total Im $\chi_2^{(111)}(\omega)$. It is clear from the results that each of the ω and 2ω resonances can be further separated into inter-band and intra-band contributions as shown in Fig. 9(d).

4 Conclusions

The effect of SOI on the optoelectronic, linear, and nonlinear optical properties of $CsPbCO_3F$ is thoroughly investigated by means of density functional theory. The electronic band gaps calculated with the inclusion of SOI effects at the TB-mBJ level of accuracy are in good agreement with the experimental reported results. The band gap results without SO effects are in good agreement with the previously reported works. The electronic band structure analysis reveals that $CsPbCO_3F$ is a direct band gap NLO material but not an indirect one as is the case when SOI is neglected. The band gap occurs at the H high symmetry point in the first Brillouin zone. Analysis of individual atomic contributions to the band structure reveals the fact that a band gap reduction of 1.1 eV for $CsPbCO_3F$ mainly occurs due to Pb atom p-states splitting near the Fermi level. More splitting of energy levels is observed in the valence and conduction bands because of SOI effects. Similar shifts are observed in the calculated PDOS plots too. Our further analysis of the charge density plots along the [1 1 0] and [1 0 1] planes reveals the mixed ionic and covalent nature of bonding present in $CsPbCO_3F$. Our further calculations on the linear optical properties (the absorption, real and imaginary parts of the dielectric function, ordinary and extraordinary refractive indices, and birefringence) also show considerable differences in the results obtained before and after the inclusion of SOI into the calculations. Our further observations about the optical transitions associated with this material show important changes with respect to SO effects. These differences alone decide the importance of SO effects for understanding the optical response of $CsPbCO_3F$. $CsPbCO_3F$ is the best phase-matching material in the deep-UV region with the highest static birefringence value of 0.1049 among all the other reported carbonate fluorides. Moreover, the present Born effective charge analysis suggests that Cs and Rb atoms show a negative contribution to the birefringence, whereas Pb, C, and F atoms positively contribute to the birefringence. Based on these important observations, we have calculated the nonlinear optical responses of $CsPbCO_3F$ using the FP-LAPW method and clearly explained the different nonlinear optical responses. The obtained $d_{11} = d_{12} = 2.35$ pm V^{-1} (static) and 4.35 pm V^{-1} (at λ = 1064 nm) values again confirm that $CsPbCO_3F$ has the highest SHG response among the carbonate family. We strongly believe that our present study on the optoelectronic, linear, and nonlinear optical properties is very crucial in understanding the structure–property correlation of the carbonate fluoride family. We hope our present results will inspire many experimental researchers to look into the uniqueness of the $CsPbCO_3F$ crystal and to invent many more efficient crystals in the carbonate fluoride family.

Conflicts of interest

There are no conflicts to declare.

Acknowledgements

ENR would like to thank DRDO (through ACRHEM under DRDO:vide project no. DRDO/02/0201/2011/00060 Phase-II) and GV would like to thank the Department of Science and Technology (DST) (under the grant SR/FTP/PS-096/2010(G)) for financial support. We would also like to acknowledge CMSD, University of Hyderabad, for providing computational facilities. AHR would like to acknowledge the CENTEM project, registered number CZ.1.05/2.1.00/03.0088, co-funded by the ERDF as part of the Ministry of Education, Youth and Sports OP RDI program and the follow-up sustainability stage, supported through CENTEM PLUS (LO1402) by financial means from the Ministry of Education. He is also grateful for the support of the Youth and Sports under the 4National Sustainability Programme I, and MetaCentrum (LM2010005) and CERIT-SC (CZ.1.05/3.2.00/08.0144) infrastructures. SA would like to thank the High Performance Facilities (HPC) at the Inter-University Accelerator Centre (IUAC) at New Delhi, the Indian Institute of Mathematical Sciences (IMSC) at Chennai, CSIR-4PI at Bangaluru, the Indian Institute of Technology at Kanpur and the University of Hyderabad in Hyderabad.

References

1 R. Arun Kumar, *J. Chem.*, 2013, (1–6), 154862.
2 R. W. Boyd, *Nonlinear Optics*, Elsevier, New York USA, 2nd edn, 2003.
3 M. A. Startsev and A. Y. Elezzabi, *ISRN Opt.*, 2013, (1–8), 419507.
4 T. T. Tran, H. Yu, J. M. Rondinelli, K. R. Poeppelmeier and P. S. Halasyamani, *Chem. Mater.*, 2016, **28**, 5238–5258.
5 M. Ouwerkerk, *Adv. Mater.*, 1991, **3**, 399–401.
6 C. T. Chen, L. Bai, Z. Z. Wang and R. K. Li, *J. Cryst. Growth*, 2006, **292**, 169–178.
7 C.-L. Hu and J.-G. Mao, *Coord. Chem. Rev.*, 2015, **288**, 1–17.
8 P. Shan, T. Sun, H. Chen, H. Liu, S. Chen, X. Liu, Y. Kong and J. Xu, *Sci. Rep.*, 2016, **6**, 25201.
9 G. Zou, N. Ye, L. Huang and X. Lin, *J. Am. Chem. Soc.*, 2011, **133**, 20001–20007.

10 G. Zou, L. Huang, N. Ye, C. Lin, W. Cheng and H. Huang, *J. Am. Chem. Soc.*, 2013, **135**, 18560–18566.
11 T. T. Tran, P. S. Halasyamani and J. M. Rondinelli, *Inorg. Chem.*, 2014, **53**, 6241–6251.
12 G. Yang, G. Peng, N. Ye, J. Wang, M. Luo, T. Yan and Y. Zhou, *Chem. Mater.*, 2015, **27**, 7520–7530.
13 T. T. Tran, J. He, J. M. Rondinelli and P. S. Halasyamani, *J. Am. Chem. Soc.*, 2015, **137**, 10504–10507.
14 Y. Lin, C.-L. Hu and J.-G. Mao, *Inorg. Chem.*, 2015, **54**, 10407–10414.
15 M. Luo, Y. Song, C. Lin, N. Ye, W. Cheng and X. Long, *Chem. Mater.*, 2016, **28**, 2301–2307.
16 L. Kang, S. Luo, H. Huang, N. Ye, Z. Lin, J. Qin and C. Chen, *J. Phys. Chem. C*, 2013, **117**, 25684–25692.
17 T. T. Tran and P. S. Halasyamani, *Inorg. Chem.*, 2013, **52**, 2466–2473.
18 L. Liu, Y. Yang, X. Dong, B. Zhang, Y. Wang, Z. Yang and S. Pan, *Chem. – Eur. J.*, 2016, **22**, 2944–2954.
19 Q. Li, G. Zou, C. Lin and N. Ye, *New J. Chem.*, 2016, **40**, 2243–2248.
20 M. Abudoureheman, L. Wang, X. Zhang, H. Yu, Z. Yang, C. Lei, J. Han and S. Pan, *Inorg. Chem.*, 2015, **54**, 4138–4142.
21 J. Chen, M. Luo and N. Ye, *Z. Anorg. Allg. Chem.*, 2015, **641**, 460–463.
22 G. Zou, G. Nam, H. G. Kim, H. Jo, T.-S. You and K. M. Ok, *RSC Adv.*, 2015, **5**, 84754–84761.
23 M. Luo, G. Wang, C. Lin, N. Ye, Y. Zhou and W. Cheng, *Inorg. Chem.*, 2014, **53**, 8098–8104.
24 E. Narsimha Rao, G. Vaitheeswaran, A. H. Reshak and S. Auluck, *RSC Adv.*, 2016, **6**, 99885–99897.
25 M. J. Verstraete, M. Torrent, F. Jollet, G. Zérah and X. Gonze, *Phys. Rev. B: Condens. Matter Mater. Phys.*, 2008, **78**, 045119.
26 P. Blaha, K. Schwarz, G. K. H. Madsen, D. Kvasnicka and J. Luitz, *WIEN2K, An Augmented Plane Wave + Local Orbitals Program for Calculating Crystal Properties*, Karlheinz Schwarz, Techn. Universität Wien, Austria, 2001, ISBN 3-9501031-1-2.
27 F. Tran and P. Blaha, *Phys. Rev. Lett.*, 2009, **102**, 226401.
28 A. Bala, T. Nautiyal and S. Auluck, *J. Appl. Phys.*, 2008, **104**(1–8), 014302.
29 J. Kuneš, P. Novák, R. Schmid, P. Blaha and K. Schwarz, *Phys. Rev. B: Condens. Matter Mater. Phys.*, 2001, **64**(1–3), 153102.
30 Q. Jing, G. Yang, J. Hou, M. Sun and H. Cao, *J. Solid State Chem.*, 2016, **244**, 69–74.
31 A. Manchon, H. C. Koo, J. Nitta, S. M. Frolov and R. A. Duine, *Nat. Mater.*, 2015, **14**, 871–882.
32 J. P. Perdew, K. Burke and M. Ernzerhof, *Phys. Rev. Lett.*, 1996, **77**, 3865–3868.
33 J. P. Perdew, A. Ruzsinszky, G. B. I. Csonka, O. A. Vydrov, G. E. Scuseria, L. A. Constantin, X. Zhou and K. Burke, *Phys. Rev. Lett.*, 2009, **102**, 039902.
34 S. Kumar, P. Suman and S. Auluck, *Adv. Opt. Mater.*, 2014, **2**, 10–17.
35 X. Luo, M. B. Sullivan and S. Y. Quek, *Phys. Rev. B: Condens. Matter Mater. Phys.*, 2012, **86**(1–15), 184111.
36 N. V. Smith, *Phys. Rev. B: Condens. Matter Mater. Phys.*, 1971, **3**, 1862–1878.
37 C. Ambrosch-Draxl and J. O. Sofo, *Comput. Phys. Commun.*, 2006, **175**, 1–14.
38 M. Fox, *Optical Properties of Solids*, Oxford University Press, New york, 2001.
39 E. Narsimha Rao, S. Appalakondaiah, N. Yedukondalu and G. Vaitheeswaran, *J. Solid State Chem.*, 2014, **212**, 171–179.
40 L. Zheshuai, X. Jiang, L. Kang, P. Gong, S. Luo and L. Ming-Hsien, *J. Phys. D: Appl. Phys.*, 2014, **47**, 253001.
41 M. Luo, C. Lin, G. Zou, N. Ye and W. Cheng, *CrystEngComm*, 2014, **16**, 4414–4421.
42 L. Kang, Z. Lin, J. Qin and C. Chen, *Sci. Rep.*, 2013, **3**(1–5), 1366.
43 X. Jiang, L. Kang, S. Luo, P. Gong, M.-H. Lee and Z. Lin, *Int. J. Mod. Phys. B*, 2014, **28**(1–27), 1430018.
44 N. Ye, Q. Chen, B. Wu and C. Chen, *J. Appl. Phys.*, 1998, **84**, 555–558.
45 S. Sharma, J. K. Dewhurst and C. Ambrosch-Draxl, *Phys. Rev. B: Condens. Matter Mater. Phys.*, 2003, **67**, 165332.
46 S. N. Rashkeev, W. R. L. Lambrecht and B. Segall, *Phys. Rev. B: Condens. Matter Mater. Phys.*, 1998, **57**, 3905–3919.
47 J. L. P. Hughes and J. E. Sipe, *Phys. Rev. B: Condens. Matter Mater. Phys.*, 1996, **53**, 10751–10763.
48 V. I. Gavrilenko, *Phys. Status Solidi A*, 2001, **188**, 1267–1280.
49 C. Ambrosch-Draxl and J. O. Sofo, *Comput. Phys. Commun.*, 2006, **175**, 1–14.
50 D. E. Aspnes, *Phys. Rev. B: Condens. Matter Mater. Phys.*, 1972, **6**, 4648–4659.
51 R. C. Eckardt, H. Masuda, Y. X. Fan and R. L. Byer, *IEEE J. Quantum Electron.*, 1990, **26**, 922–933.
52 K. Zhang and X. Wang, *Chin. Sci. Bull.*, 2001, **46**, 2028–2036.
53 http://www.castech-us.com/casktp.htm.
54 M. V. Pack, D. J. Armstrong and A. V. Smith, *Appl. Opt.*, 2004, **43**, 3319–3323.
55 I. Shoji, T. Kondo, A. Kitamoto, M. Shirane and R. Ito, *J. Opt. Soc. Am. B*, 1997, **14**, 2268–2294.
56 A. Anema and T. Rasing, *Appl. Opt.*, 1997, **36**, 5902–5904.
57 L. K. Cheng, L. T. Cheng, J. Galperin, P. A. M. Hotsenpiller and J. D. Bierlein, *J. Cryst. Growth*, 1994, **137**, 107–115.
58 H. Vanherzeele and J. D. Bierlein, *Opt. Lett.*, 1992, **17**, 982–984.
59 B. Boulanger, J. P. Fve, G. Marnier and B. Mnaert, *J. Opt. A: Pure Appl. Opt.*, 1998, **7**, 239.
60 A. H. Reshak, I. V. Kityk and S. Auluck, *J. Phys. Chem. B*, 2010, **114**, 16705–16712.
61 Q. Bian, Z. Yang, L. Dong, S. Pan, H. Zhang, H. Wu, H. Yu, W. Zhao and Q. Jing, *J. Phys. Chem. C*, 2014, **118**, 25651–25657.

